COMMUNICATIONS CHEMISTRY

ARTICLE

DOI: 10.1038/s42004-018-0049-4 OPEN

Nucleation of quartz under ambient conditions

Phil Buckley[1], Natasha Hargreaves[1] & Sharon Cooper[1]

Quartz nucleation normally requires harsh conditions; for instance, hydrothermal processes at 200–300 °C and 15–100 bar, where the high growth rate precludes selective formation of nanometer-sized quartz. Under ambient conditions, even quartz growth is considered to occur exceedingly slowly, requiring yearly timescales. Here we show that nanoquartz of size 1–5 nm can be nucleated from microemulsions under ambient conditions within 2 days. The nanoquartz particles are grown and annealed under mild hydrothermal conditions of 175 °C and autogenic pressure. This enables nanoquartz of size <10 nm and controllable structure to be obtained exclusively. Surface defects play a key role in determining the catalytic properties of the nanoquartz. Consequently, a similar two-stage microemulsion-hydrothermal synthesis strategy could provide significant benefits in optimizing nanocrystal catalysts.

[1] Department of Chemistry, Durham University, Lower Mountjoy, Stockton Road, Durham DH1 3LE, UK. Correspondence and requests for materials should be addressed to S.C. (email: sharon.cooper@durham.ac.uk)

Quartz is an abundant material in the Earth's soil and crust, forming from molten magmas at 800 °C and hydrothermal veins at temperatures of 250 to 450 °C. Synthetic quartz is often produced by hydrothermal and solvothermal methods[1–4], though solid-state transformation of amorphous silica to quartz is also possible at >600 °C[5–7]. In contrast, obtaining quartz under ambient conditions is exceedingly difficult; crystalline silica has been produced by a biological route involving the fungus *Fusarium oxysporum*, but the nanocrystals contained significant quantities of occluded proteins[8]. Primary nucleation of quartz under ambient conditions by non-biological routes has never been reported to our knowledge. Indeed, even secondary nucleation and growth on existing α-quartz crystals under ambient conditions is exceedingly slow, requiring yearly timescales[9]. Instead, the main silica phase precipitating under ambient temperature and pressure is amorphous silica, exemplified by natural biosilification processes and the Stöber reaction[10], which can produce nearly monodisperse amorphous silica spheres[11].

Here we report the formation of α-quartz nanocrystals of size 1–5 nm from water-in-oil microemulsions under ambient conditions within 2 days using aqueous sodium metasilicate (pH 12–13) as the silica precursor. Recently it has been shown that microemulsions can induce thermodynamic control of crystallization in organic crystals[12–16]. We show here that microemulsions can elicit the same thermodynamic control in crystallizing silica, a giant covalent structure, even though this requires the creation and breaking of much stronger covalent bonds compared to the intermolecular bonds in organic crystals. Si–O bond cleavage/formation is catalyzed at high/low pH. We hypothesize that it is the diversity of the local pH environment arising from the presence or absence of hydroxyl and far rarer hydronium ions in the isolated droplets that enables both Si–O bond cleavage and formation to occur repeatedly on the 2-day timescale of the microemulsion experiments. We propose that this helps ensure near-equilibration and hence thermodynamic control. Microemulsions and emulsions have been used previously to produce amorphous silica under ambient conditions[17–20] but never α-quartz. Our finding that quartz nucleation is achievable under ambient conditions by using nanoconfinement challenges the common preconception that nanoquartz deposits are a signature of high temperature and pressure conditions.

The microemulsion-extracted α-quartz nanocrystals are then used to seed hydrothermal syntheses under mild conditions of 175 °C and autogenic pressure (nominally ≈9 bar). This enables nanoquartz of defined size (< 10 nm) to be obtained exclusively for the first time. Shorter hydrothermal synthesis times produce nanoquartz crystals with a perturbed α-quartz structure and more surface and interior defects, which dissolve and anneal out, respectively, after longer hydrothermal times of up to 7 days to produce the expected α-quartz structure. Such nanocrystals will be ideal for studies aimed at minimizing silicosis and other lung diseases where respiratory nanoquartz has been implicated, particularly given recent suggestions that it is surface disorder on quartz nanocrystals that helps induce cell toxicity[21]. Amorphous silica is known to catalyze the reaction of β-diketones and amines to form β-enaminones, which are important organic intermediates. We use the nanocrystals to affect the yield of the β-enaminone, 4-(phenylamino)-pent-3-en-2-one, produced from acetylacetone and aniline. Contrasting results are obtained dependent on the nanoquartz structure. Nanoparticulate catalysts are vital in heterogeneous catalysis. Our two-stage microemulsion-hydrothermal synthesis methodology can provide significant control over the size and surface structure of nanocrystals to help optimize their catalytic performance.

Results

Nanoquartz from microemulsions. TEM studies on Span® 80 and Brij® 30 (SB) microemulsion aliquots established the formation of α-quartz nanocrystals as the majority silica phase present in microemulsions containing 5 μl g^{-1} sodium metasilicate (SMS) solutions of <10 wt.%. The size of the nanocrystals after 2 days ranged from 1–5 nm, with a mean size of 2.0 ± 0.7 nm (based on the sizing of 550 particles in TEM micrographs); after 9 days, some aggregation had occurred and this enabled electron diffraction patterns to be observed, albeit weakly, above the diffuse rings of the amorphous holey carbon grid background (see Fig. 1, Table 1, Supplementary Fig. 1 and Supplementary Table 1). Analysis of the diffraction patterns revealed spacings of 0.34, 0.24, 0.20, and 0.17 nm, consistent with diffraction from $\{\bar{1}01\}$, $\{1\bar{2}0\}$, $\{02\bar{1}\}$, and $\{\bar{2}02\}$ α-quartz planes, respectively, which are all part of the ⟨212⟩ zone axes. The presence of the 0.34 nm spacing established that there must be nanoquartz present since silicon and cristobalite have no interplanar distances close to this spacing. In addition, 0.31 and 0.19 nm spacings were observed, attributable to the {111} and {220} strongest diffracting planes of silicon, since it is known that α-quartz can beam damage and reduce to silicon under even relatively low intensity electron beams[22]. Silicon and oxygen peaks were present in the EDX patterns but there was no sodium peak (Supplementary Fig. 1), confirming that the nanocrystals were not sodium silicate.

Fast Fourier Transforms (FFTs) from high resolution nanocrystal images revealed the same diffraction spacings of 0.20 and 0.17 nm attributable to the α-quartz ⟨212⟩ zone axes (see Table 2). The ⟨212⟩ zone axes correspond to the quartz nanocrystals lying on, or close to, the low energy rhombohedral {101} faces. The {101} faces have a large proportion of Q^3 Si–OH silanol surface sites, i.e. a silicon atom bonded to three 3 bridging oxygen atoms and one Si–OH surface bond, rather than Q^2 Si–$(OH)_2$ sites[23]. This aids their thermodynamic stability and is consistent with the proposed model of the crystallization being under thermodynamic control.

On increasing the SMS amount in the aqueous phase to 10 wt. %, cristobalite emerged as the predominant silica phase, with fewer α-quartz nanocrystals observed (Fig. 2). At 14 wt.% SMS, the majority phase was amorphous silica in the form of distinctive, larger spheres (Fig. 2c). Similarly, on increasing the volume of the SMS dispersed phase from 5 μl g^{-1} to 50 μl g^{-1}, α-quartz became a minority phase even at 1 wt.% SMS whilst cristobalite was the majority phase (Supplementary Fig. 2).

Changing the surfactant system from Span® 80 and Brij® 30 to Triton X-114 (TX) yielded entirely analogous results establishing that the predominant polymorph is controlled by the SMS concentration and droplet size and not the surfactant chemistry. In particular, low wt.% SMS (<10 wt.%) and low dispersed phase volumes of 5 μl g^{-1} produce predominantly α-quartz of size 1–5 nm (Fig. 3); increased wt.% SMS and dispersed phase volumes up to 50 μl g^{-1} result in increasing amounts of cristobalite and larger amorphous silica spheres (Supplementary Fig. 3).

Small Angle X-ray Scattering (SAXS) and GIFT analysis[24] was used to size the microemulsion droplets (see Supplementary Fig. 4 and Supplementary Tables 2 to 5). The droplets' mean hydrophilic core radius increased from 1.5 nm to 2.7 nm as the SMS solution volume increased from 5 μl g^{-1} to 50 μl g^{-1} for the Span®80 Brij®30 (SB) microemulsions. These values are consistent with those of other SB microemulsions[12,13]. For the Triton X-114 (TX) microemulsions, the droplets' mean hydrophilic core radius increased from 1.9 nm to 2.9 nm as the SMS solution volume increased from 5 μl g^{-1} to 50 μl g^{-1}. These droplet sizes suggest that the nanoquartz and smaller cristobalite nanocrystals

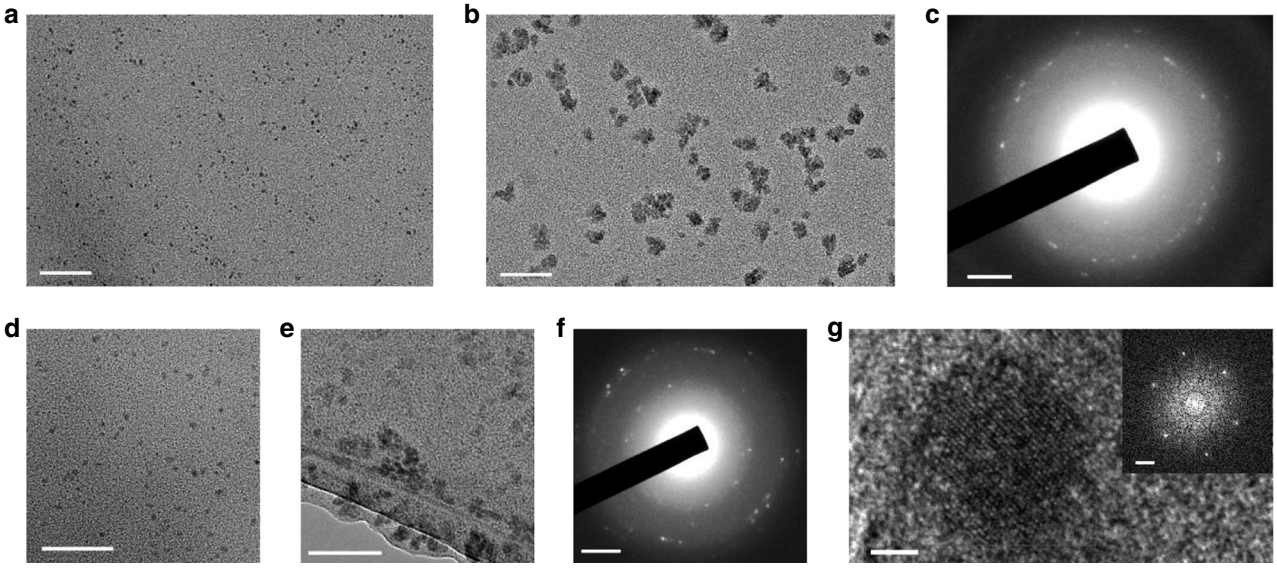

Fig. 1 Nanoquartz synthesized from SB microemulsions. Representative TEM data of the nanoquartz synthesized from SB (Span® 80 and Brij® 30) microemulsions using 5 μl g^{-1} of a 3 wt.% (**a**–**c**), 5 wt.% (**d**) and 7.5 wt.% (**e**–**g**) aqueous SMS (sodium metasilicate) solution. **a**, **b** Bright field images of 1–5 nm particles formed after standing the microemulsion for **a** 2 days and **b** 9 days. **c** Electron diffraction pattern of the region shown in **b** revealing diffraction spots attributed to α-quartz and silicon, see Table 1. **d**, **e** Bright field images of 1–5 nm particles formed after standing the microemulsion for **d** 2 days and **e** 9 days. **f** Electron diffraction pattern of the region shown in **e** revealing diffraction spots attributed to α-quartz and silicon, see Table 1. **g** High resolution image (HREM) of a 5 nm particle after standing the microemulsion for 2 days. The inset shows the FFT of the image, which indexes on the ⟨212⟩ zone axis of α-quartz. Scale bars are 50 nm in **a**, **b**, **d**, and **e**, 5 nm in **g** and 2 nm^{-1} in **c**, **f** and the inset to **g**

Table 1 Diffraction spacings and assignments for diffraction patterns

Electron diffraction from 3.0 wt.% aqueous SMS microemulsion (Fig. 1c)		Electron diffraction from 7.5 wt.% aqueous SMS microemulsion (Fig. 1f)	
Measured d-spacing (nm)	**Assignment**	**Measured d-spacing (nm)**	**Assignment**
0.172[a]	α-Quartz {$\bar{2}02$} at 0.167 nm	0.172[a]	α-Quartz {$\bar{2}02$} at 0.167 nm
		0.192	Silicon {220} at 0.192 nm
0.197	α-Quartz {$02\bar{1}$} at 0.198 nm	0.200	α-Quartz {$02\bar{1}$} at 0.198 nm
0.311	Silicon {111} at 0.314 nm	0.311	Silicon {111} at 0.314 nm
		0.339[a]	α-Quartz {$\bar{1}01$} at 0.334 nm

[a]These spacings are slightly larger than the bulk α-quartz spacings. This may just reflect the uncertainty in the measurements or it may be indicative of a slightly perturbed quartz structure for the nanocrystals. The latter would be in agreement with our hydrothermal studies, where XRD analysis showed the nanoquartz obtained after 1–5 days also contained perturbed structures, with {101} spacings of 0.340 nm

Table 2 ⟨212⟩ zone axes of quartz

Zone axis	d-spacings (nm)			Angles (°)		
⟨212⟩	0.198 {$02\bar{1}$}	0.198 {$\bar{2}21$}	0.167 {$\bar{2}02$}	72.6 ∠{$02\bar{1}$} {$\bar{2}21$}	53.7 ∠{$\bar{2}21$} {$\bar{2}02$}	53.7 ∠{$02\bar{1}$} {$\bar{2}02$}

(see Supplementary Fig. 2d) were confined within the droplets during their nucleation and growth. In contrast, the amorphous silica spheres and larger cristobalite crystals could continue to grow to sizes much larger than the mean droplet size owing to the greater SMS concentration in the microemulsion droplets, with latter-stage growth involving droplet rupture to release aqueous SMS onto the larger particle surfaces.

Nanoquartz with a perturbed bulk structure. On our normal 2-gram microemulsion scale, the maximum quantity of α-quartz nanocrystals that could be obtained was <0.1 mg, given that <10 wt.% aqueous SMS was needed to produce predominantly α-quartz. Consequently, larger scale 400 g microemulsions were prepared containing 2.5 wt.% SMS solution to extract sufficient α-quartz nanocrystals for XRD, FTIR and ^{29}Si ssNMR analysis. Centrifuging at 9418 G was ineffective at sedimenting the 1–5 nm particles from the microemulsions. Instead, the SB microemulsions were left for 2 weeks for nanoquartz aggregation and subsequent sedimentation to occur. XRD analysis on the resulting white powders revealed a broad hump at $2\theta = 22°$, however, which appears to be more consistent with amorphous silica than a crystalline phase (Fig. 4a). The breadth of the hump suggests the broadening arises not only from the small 1–5 nm crystallite size, but from variations in the lattice positions, i.e. the nanoquartz has a slightly perturbed bulk α-quartz structure and may contain interior defects. FITR analysis showed a significant Si–OH

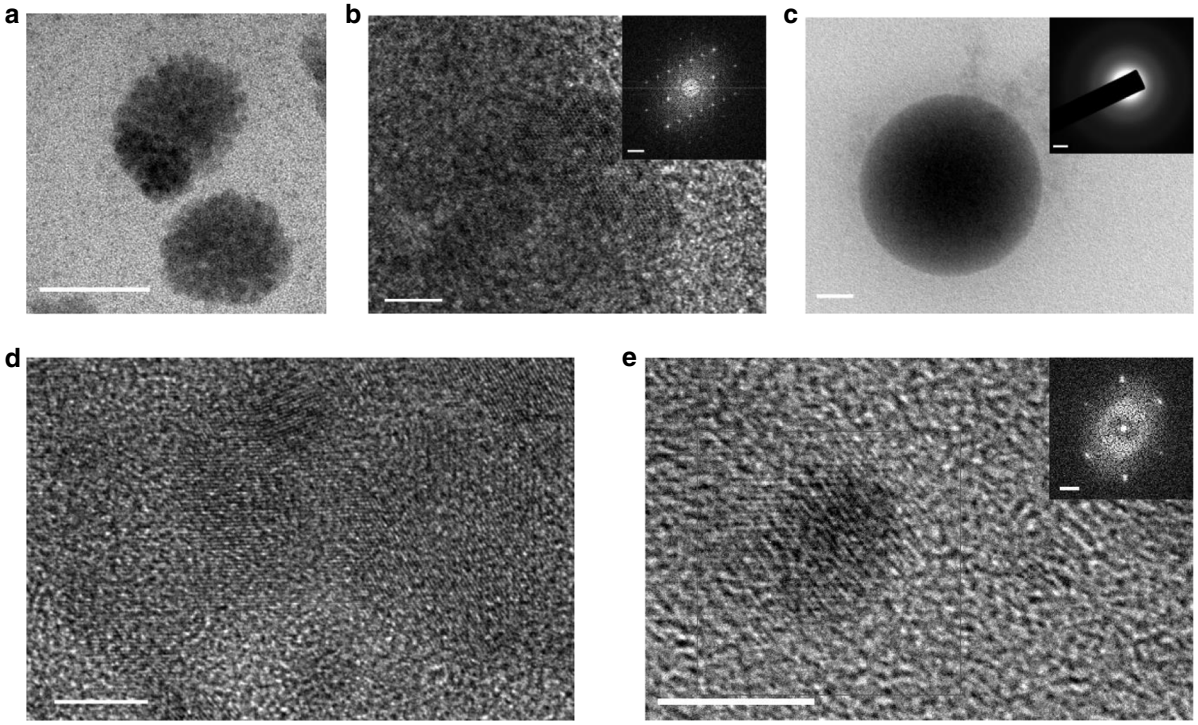

Fig. 2 Crystalline and amorphous silica from higher SMS concentration SB microemulsions. Representative TEM of the silica phases synthesized from SB (Span® 80 and Brij® 30) microemulsions after 2 days using 5 μl g^{-1} of a 10 wt.% (**a**, **b** and **d**) and a 14 wt.% (**c**, **e**) aqueous SMS (sodium metasilicate) solution. **a** HREM image of ≈50 nm cristobalite particles. **b** Higher magnification image of the lower particle shown in **a**. The inset shows the FFT, which indexes on the ⟨110⟩ zone axis of cristobalite. **c** Representative amorphous silica material, which formed the majority silica phase for the 14 wt.% aqueous SMS microemulsion. The inset shows the particle's electron diffraction pattern and absence of sharp diffraction spots. **d** HREM image of a cluster of ≈2–10 nm particles, with some showing lattice fringes. **e** HREM image of a 5 nm particle. The inset shows the FFT, which indexes on the ⟨212⟩ zone axis of α-quartz. Scale bars are 50 nm in **a** and **c**, 5 nm in **b**, **d** and **e** and 2 nm^{-1} in the insets to **b**, **c** and **e**

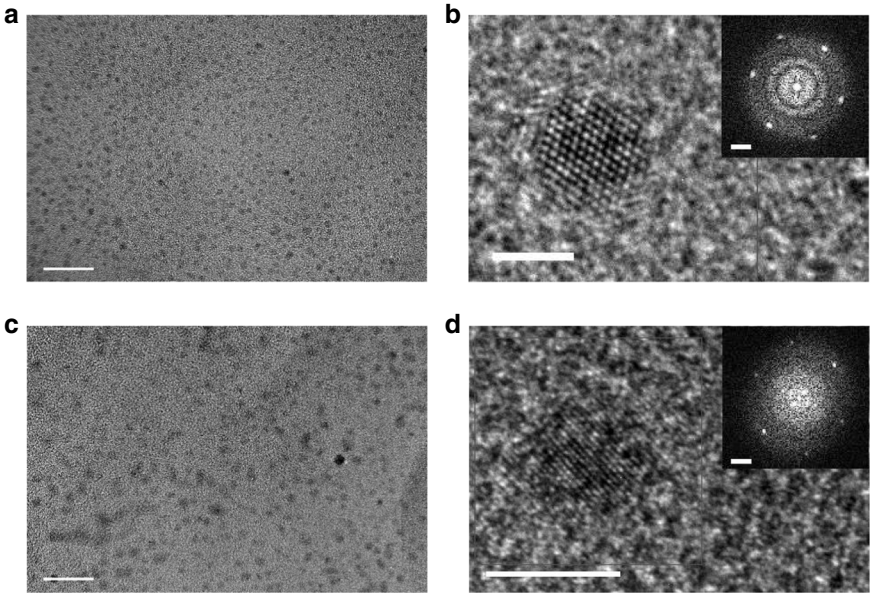

Fig. 3 Nanoquartz synthesized from TX microemulsions. Representative TEM data of the nanoquartz synthesized from TX (Triton X-114) microemulsions after 2 days using 5 μl g^{-1} of a 4 wt.% aqueous SMS (sodium metasilicate) solution (**a**, **b**) and 5 μl g^{-1} of a 6 wt.% aqueous SMS solution (**c**, **d**). **a** Bright field image of 1–5 nm particles. **b** HREM image of a 3 nm particle. The inset shows the FFT, which indexes on the ⟨212⟩ zone axis of α-quartz. **c** Bright field image of 1–5 nm particles. **d** HREM image of a 5 nm particle. The inset shows the FFT, which indexes on the ⟨212⟩ zone axis of α-quartz. The scale bars are 20 nm in **a** and **c**; 2 nm in **b**, 5 nm in **d** and 2 nm^{-1} in the insets to **b** and **d**

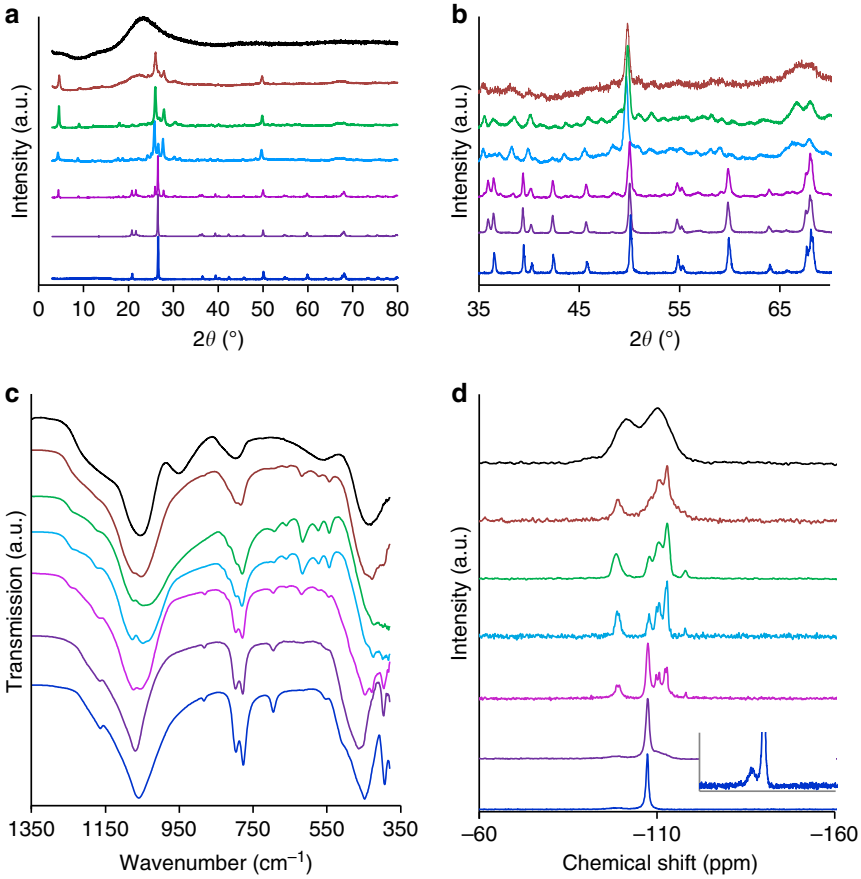

Fig. 4 Analysis of the nanoquartz. **a** and **b** XRD, **c** FTIR, and **d** ^{29}Si ssNMR data of the microemulsion-synthesized nanoquartz (black lines) and the products from 1-day (brown lines), 2-day (light green lines), 3-day (light blue lines), 5-day (pink lines), 6-day (purple lines), and 7-day (blue lines) hydrothermal synthesis at 175 °C. **b** provides a more-detailed view of the 1–7 day hydrothermal XRD data between $2\theta = 35$–$70°$, to better show the weaker peaks. The inset in **d** shows an expanded view of the 7-day ^{29}Si ssNMR spectrum, revealing the small, broad Q^3 Si–OH peak at −99 ppm. Q^4 Si–O peaks appear at −107 to −118 ppm, Q^3 Si–OH peaks at −99 to −101 ppm and Q^2 $Si(OH)_2$ peaks at −92 ppm

peak at 950 cm^{-1} along with prominent Si–O–Si peaks at 1060 cm^{-1}, 800 cm^{-1} and 435 cm^{-1} (Fig. 4c) and a broad OH stretch centred at 3350 cm^{-1}. In addition, ^{29}Si ssNMR revealed peaks at −92, −101 and −110 ppm attributable to 4.7% Q^2 $Si(OH)_2$, 35.3% Q^3 Si(OH), and 60.0% Q^4 Si (Fig. 4d). Nanocrystals of size 1-5 nm would be expected to have a large proportion of Q^3 sites due to their large surface to volume ratios, whilst the low proportion of Q^2 $Si(OH)_2$ is consistent with the nanocrystals having many surfaces along, or close to, low energy {101} planes. However, the breadth of all the ^{29}Si ssNMR peaks indicates variations in Si–O–Si angles arising from distortions of the bulk quartz structure. Note though, the Q^3 and Q^4 peaks are still narrower than that of the 7 nm fumed silica (Supplementary Fig. 5c), which, being amorphous, has larger variations in the Si–O–Si angles. TGA analysis (Supplementary Fig. 6) reveals the nanocrystals lose 27% of their mass upon heating to 800 °C; 10% is due to surface water loss before 100 °C and the remaining 17% corresponds to removal of Si–OH bonds both on the nanocrystal surface and at any defect sites within the nanocrystals.

It is clear from the lattice fringes and electron diffraction in the TEM studies that quartz-like crystallinity is present in the microemulsion-derived nanoparticles, notwithstanding the perturbations. Moreover, the formation of these 1–5 nm particles from the 2.5 wt.% SMS solution, a solution undersaturated with respect to amorphous silica, definitively establishes these nanoparticles are less soluble than amorphous silica, despite their small size, indicating improved interior bonding over amorphous silica. Solubility tests in 0.1 M NaOH corroborated this (Supplementary Table 6).

Addition of further aliquots of 2.5 wt.% SMS solution to existing 400 g scale 2.5 wt.% SMS microemulsions produced more quartz nanocrystals. This process could be repeated up to ≈12 times before the nanocrystal yield reduced significantly, presumably because of the increasing alkalinity favouring dissolution over growth. The 1–5 nm quartz nanocrystals were used as seeds in hydrothermal syntheses to obtain quartz nanocrystals of controllable size and structure.

Hydrothermal synthesis. Hydrothermal synthesis under mild conditions of 175 °C and autogenic pressure was used to anneal and slightly grow the nanoquartz obtained from the microemulsions. After 1 day of hydrothermal treatment, sharper peaks appeared in the XRD pattern of the extracted nanocrystals (Fig. 4a, b). However, the peaks at 2θ values of 26.0°, 27.9°, and 30.4° (corresponding to d- spacings of 0.34 nm, 0.32 nm, and 0.29 nm, respectively) are more consistent[25] with the moganite phase of silica rather than a bulk α-quartz structure. Quartz has its main (101) diffraction peak at $2\theta = 26.7°$ ($d =$ 0.33 nm) and has no other peaks in the $2\theta = 26$–$35°$ region. Moganite consists of alternating (101) layers of left and right-handed α-quartz helices, and therefore represents the extreme form of quartz Brazil twinning occurring on the unit cell length-scale[25]. The low angle peak at $2\theta = 4.6°$ ($d = 2.1$ nm)

and its second order peak are consistent with a quartz supercell structure containing 6 α-quartz (101) planes (see Supplementary Note 1). Accordingly, this suggests that the nanocrystals at this stage contained both left and right-handed α-quartz helices, leading to a perturbed α-quartz supercell structure with features similar to moganite. It is likely that the left and right-handed α-quartz helices were also present in the microemulsion-synthesized nanoquartz given the broadness of its XRD peak.

After 2 days of hydrothermal treatment, pre-existing peaks sharpened slightly and additional weak, relatively sharp XRD peaks appeared, again consistent with a perturbed quartz supercell that contained both left and right-handed α-quartz helices. An emerging peak at $2\theta = 26.7°$ signalled that the bulk α-quartz structure was now developing. From 3–6 days, there was an increase in the XRD peaks associated with the bulk α-quartz structure, whilst the peaks due to the perturbed supercell were decreasing. After 7 days of hydrothermal treatment, only the bulk α-quartz structure was evident (Fig. 4a, b and Supplementary Note 2).

FTIR and ^{29}Si ssNMR fully corroborated the XRD findings (Fig. 4c, d). FTIR peaks associated[26] with defective quartz and moganite at ≈660, 615, 575, and 545 cm^{-1} were apparent from 1–5 days. The α-quartz doublet at 780 and 800 cm^{-1} and the so-called "crystallinity peak" at 700 cm^{-1} emerged at 2 days. At 6 and 7 days, only the bulk α-quartz spectrum with its prominent doublet and crystallinity peak was evident.

The ^{29}Si ssNMR spectrum after 1 day shows significant narrowing of the Q^3 Si–OH peak at −100 ppm and the Q^4 Si peak has split into three components at −108, −111, and −113 ppm; the peak at −108 ppm represents the emerging bulk α-quartz structure, and the −111 and −113 ppm peaks, the perturbed α-quartz structure. In comparison, the ^{29}Si ssNMR peaks for moganite occur at −106 and −110 ppm[27]. There is no longer a Q^2 Si–$(OH)_2$ peak in the 1-day spectrum. At 2 days, a sharper Q^3 Si–OH peak at −99 ppm and 4 sharper Q^4 Si peaks at −108, −111, −113, and −118 ppm are seen. The small −118 ppm peak is most likely due to a minority of highly-strained 4-membered silica rings. From 3–5 days, the peaks sharpened and the α-quartz signal increased in intensity and shifted slightly to −107 ppm. The 6-day sample contains only 1 sharp bulk α-quartz peak at −107 ppm, together with a broad Q^3 Si–OH peak at −98 ppm mainly due to surface silicons, and a broad Q^4 Si- peak at −109 ppm reflecting the remaining perturbations to the bulk quartz structure. At 7 days, only the sharp −107 ppm bulk α-quartz signal is evident, showing that the nanocrystals had (largely) annealed. Note, however, there remains a small, broad Q^3 Si–OH peak at −99 ppm after 7 days (Fig. 4d inset), which accounts for 7.9% of the silicon atoms, consistent with their nm-size.

TEM analysis shows there is slight growth of the nanocrystals as the crystals anneal (Fig. 5). Note aggregation of the nanocrystals into larger ≈20–70 nm aggregates was common after 2 days of hydrothermal treatment (see Supplementary Fig. 7 and Supplementary Note 2). Performing the hydrothermal experiments under stirring would be expected to reduce the number of these aggregates. After 7 days, most of the crystals were still <5 nm in size; the mean size was 4.4 nm ± 0.9 nm (based on the sizing of 461 particles in TEM micrographs, see Fig. 5k); this mean value is entirely consistent with a process involving only growth and annealing of existing particles (see below), hence the microemulsion nanoquartz particles were effective seeds.

Hydrothermal synthesis yields. The yield of the hydrothermal product ranged from 144.2 mg for the 1-day hydrothermal experiment to 232.3 mg for the 7-day run; these yields being consistent with their relative solubilities. Furthermore, the relative size increase of the microemulsion seeds from 2.0 ± 0.7 nm to 4.4 ± 0.9 nm for the 7-day product (see Fig. 5) is also consistent with these yields. In particular, excluding the surface water (TGA establishes ≈10% water in the microemulsion seeds compared to ≈2% for the 7-day hydrothermal product, see Supplementary Fig. 6), this gives a SiO_2 mass increase from 51.7 mg to 227.7 mg in 7 days, i.e. by a factor of 4.4, so the particle size should increase by $\approx 4.4^{1/3} \approx 1.6$ for isotropic 3D growth and by $\approx 4.4^{1/2} \approx 2.1$ for mainly 2D growth. These values are in good agreement with our observed mean size increase of 2.2, particularly given that after 7 days, Ostwald ripening would have led to dissolution of the smallest crystals and growth of the largest. This provides further proof that the nanoquartz hydrothermal product occurs via annealing and growth of our microemulsion-derived nanoquartz seeds: a mechanism reliant on new particle nucleation and growth is certainly not occurring.

Quartz nucleation and growth at low temperature. It is well-known that the critical nucleus can possess a structure that differs from the bulk crystal phase; the structures that minimize the free energy on the nm-scale and bulk scale vary (sometimes markedly) due to the large surface contributions to the former. We consider this happens here. However, the perturbations to the bulk quartz structure are relatively minor once the nanocrystals reach >2 nm, given the electron diffraction patterns can be indexed using the bulk quartz structure and major XRD peaks of the product remain at $2\theta = 26.0–26.7°$, 49.7–50.2°, and 67.8–67.9° throughout the hydrothermal 1–7 day experiments (Fig. 4a, b).

A concomitant quartz nucleation-nanocrystal dissolution mechanism can be categorically ruled out because the nucleation rate under our hydrothermal conditions proceeds at too low a rate compared to crystal growth. A low quartz nucleation rate would result in the final product mainly consisting of fewer, but larger (μm-sized) quartz particles as previously observed[1–3]. This is borne out by our control hydrothermal experiments at 175 °C and autogenic pressure using 7 nm fumed silica rather than the microemulsion nanoquartz seeds (see below). In these control systems, the majority of the quartz crystals were μm-sized, even after 2 days (see Supplementary Fig. 8). These results highlight the effectiveness of our two-stage microemulsion-hydrothermal synthesis strategy in obtaining selective crystallization of nanoquartz of size range < 10 nm.

Control hydrothermal synthesis results using fumed silica as the seed material. In our control experiments, after 1 day at 175°C and autogenic pressure (nominally ≈9 bar), a predominantly amorphous product was obtained due to the excess fumed silica. However, the XRD of this product did contain some weak sharper peaks showing some limited nucleation had occurred (see Supplementary Fig. 5a). As expected, the FTIR and ^{29}Si ssNMR spectra of this 1-day control were similar to that of the 7 nm fumed silica (see Supplementary Figs. 5b,c), though TEM analysis confirmed the presence of some tiny <5 nm nanocrystals amongst this amorphous product (see Supplementary Fig. 8c). After 2 days, the relatively low nucleation rate meant that these nanocrystals had grown to μm-sized crystals, whilst nucleation events in the interim had led to some smaller nm-sized crystals; hence a polydisperse product was obtained (see Supplementary Fig. 8d,e). The XRD, FTIR and ^{29}Si ssNMR data revealed that the crystals possessed a similar perturbed bulk quartz structure to our 1–2 day hydrothermal nanoquartz crystals.

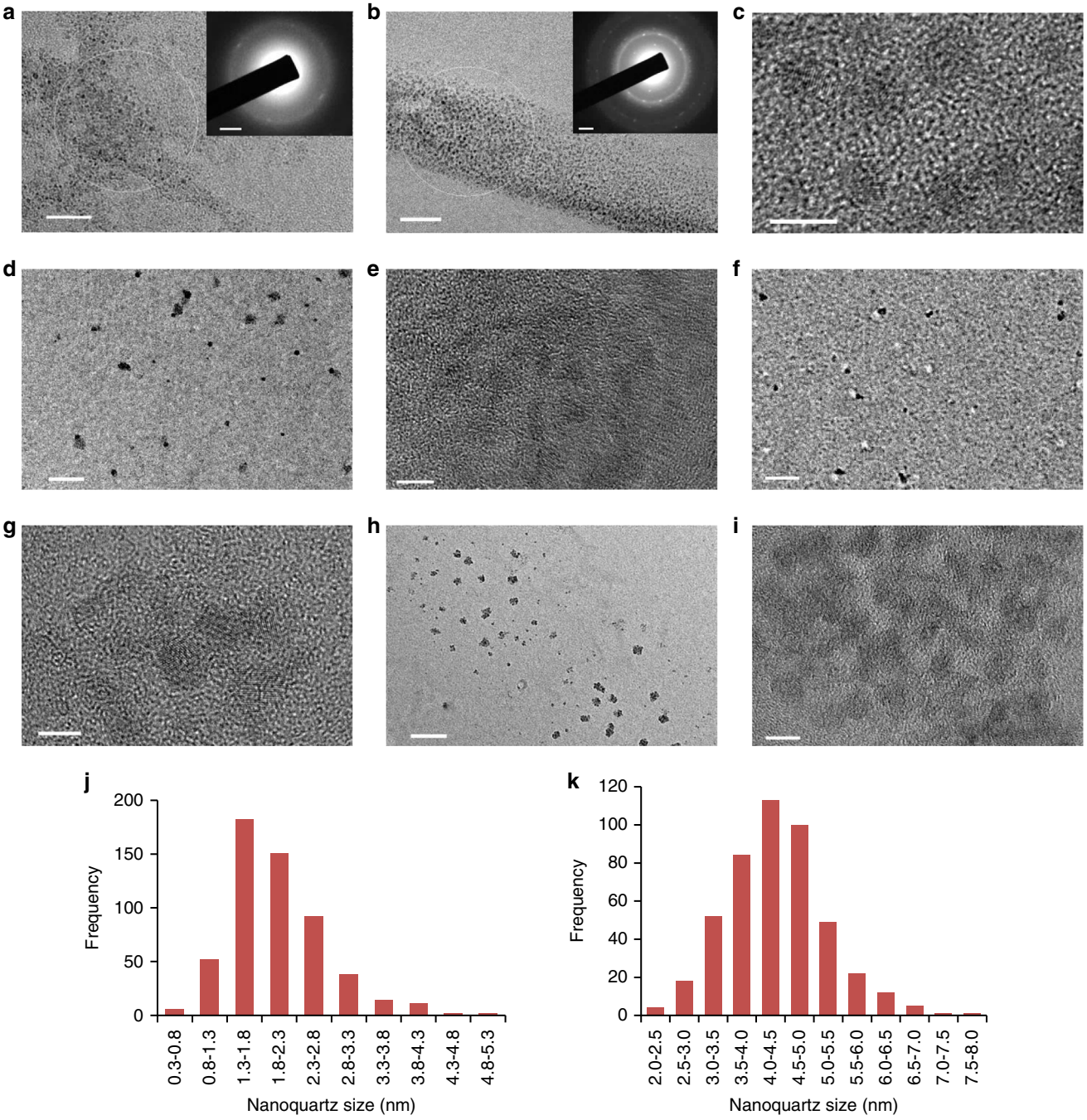

Fig. 5 Representative TEM images and data of the nanoquartz. **a** microemulsion-synthesized nanoquartz; **b**, **c** 2-day hydrothermal product; **d**, **e** 5-day hydrothermal product; **f**, **g** 6-day hydrothermal product; **h**, **i** 7-day hydrothermal product; **j** histogram showing the particle size for microemulsion-synthesized nanoquartz obtained from HREM micrographs by sizing 550 particles; **k** histogram showing the particle size for the 7-day hydrothermal product obtained from HREM micrographs by sizing 461 particles. The scale bars are 50 nm in **a** and **b**; 5 nm in **c**, **e**, **g**, and **i**; 100 nm in **d**, **f**, and **h** and 2 nm^{-1} in the insets to **a** and **b**. The insets to **a** and **b** show the electron diffraction pattern from the circled regions. The diffraction ring in **a** corresponds to 0.2 nm, consistent with the electron diffraction patterns shown in Fig. 1. The diffraction pattern in **b** has a ring pattern commensurate with quartz and inner hexagonal diffraction spots that index as (003) on a doubled quartz cell, consistent with a slightly perturbed quartz structure

The perturbed bulk structure was still evident in the product from the 5-day hydrothermal control experiment, with most crystals now being >2 μm in size. This demonstrated that, as expected, the growth process was similar to that of our nanoquartz-seeded hydrothermal experiments, albeit the growth was somewhat delayed due to the nucleation time-lag, and this low nucleation rate then meant that fewer but much larger, μm-sized crystals developed. The much larger crystal sizes resulted in reduced solubilities compared to the analogous nanoquartz-seeded experiments (see Supplementary Table 6). After 7 days in the control experiments, the bulk quartz crystal structure was observed using XRD, FTIR, and ^{29}Si ssNMR but by this stage, most crystals were ≥3 μm in size (see Supplementary Figs. 5 and 8i) and had a solubility 61% lower than the 7-day hydrothermal nanoquartz-seeded sample.

Catalyst performance. Amorphous silica is known to catalyze the formation of β-enaminones, an important class of synthons for the production of various heterocyclic and pharmaceutical compounds. The effect of the fumed silica and quartz nanoparticles on the reaction between acetylacetone and aniline to form the β-enaminone, 4-(phenylamino)-pent-3-en-2-one[28,29] was investigated (see Table 3). The 7 nm fumed silica was an effective catalyst, in agreement with previous studies in which the catalytic ability was linked to absorption of acetylacetone onto silanol sites[28,29]. This facilitates the nucleophilic attack of the amine to generate the imine intermediate followed by tautomerization to the corresponding β-enaminone. The microemulsion-synthesized nanoquartz, with its perturbed quartz structure, only weakly catalyzed the reaction. This is surprising, given it contained comparable amounts of silanol groups to the 7 nm fumed silica. Furthermore, a strong inhibitory effect was observed for the hydrothermal nanoquartz crystals, with the annealed 7-day hydrothermal nanoquartz causing extreme inhibition. The precise origin of this inhibition requires further study and residual alkalinity (at a level too low to impact the 9:2 enol:keto ratio) in the hydrothermal quartz samples may play a part. Nevertheless, given that reaction rates for the 7-day hydrothermal nanoquartz system are increased significantly when excess acetylacetone is used, but markedly less so with excess aniline, this suggests adsorption of the acetylacetone onto the annealed nanoquartz occurs in a manner discordant with subsequent β-enaminone formation. In comparison, the control 5–7 day hydrothermal quartz crystals had a more limited inhibitory effect, owing to their μm size and reduced surface area. Accordingly, the catalyst performance findings are consistent with inhibition increasing as the perturbed nanoquartz structure anneals to that of α-quartz. This finding emphasizes the need for careful control over the synthesis of nanoparticulate catalysts to ensure effective performance.

Table 3 Product yields for the reaction between acetylacetone and aniline

Silica phase added as a potential catalyst	% Yield of product, 4-(phenylamino)-pent-3-en-2-one[a]		
	4 h	5 h	6 h
7 nm fumed silica	70±1	76±2	81±2
200–300 nm fumed silica	59	67	74
Microemulsion-synthesized nanoquartz	45±5	54±4	60±4
Microemulsion-synthesized nanoquartz, excess (100 μl) SB surfactant mixture	47.4	54.9	61.3
Quartz standard with mean crystal size ≈350 μm by mass	31.9	42.4	53.8
None	31±2	42±4	52±5
1-day hydrothermal nanoquartz	8±1	12±4	16±6
5-day hydrothermal nanoquartz	11±4	15±4	19±6
6-day hydrothermal nanoquartz	18±1	25±1	32±1
7-day hydrothermal nanoquartz	3.9±0.1	5.2±0.2	7.1±0.5
7-day hydrothermal nanoquartz, 300% excess aniline	10.5	11.3	13.1
7-day hydrothermal nanoquartz, 300% excess acetylacetone	25.4	40.5	53.2
Control 1-day hydrothermal quartz	9.2	13.5	17.6
Control 5-day hydrothermal quartz	12.9	19.3	26.1
Control 6-day hydrothermal quartz	15.8	26.5	38.3
Control 7-day hydrothermal quartz	24.7	36	47.6

[a]Experiments showing standard deviations were repeated at least twice. Values without standard deviations were from single experiments. The 7 nm fumed silica and no catalyst experiments were performed in each batch of experiments to ensure reproducibility of results.

Discussion

α-quartz nanocrystals have been produced in 2 days at ambient temperature by using a microemulsion-mediated methodology. Previous studies have demonstrated the ability of microemulsions to elicit thermodynamic control over crystallization for organic molecular crystals[12–16] but this is the first time thermodynamic control has been achieved for a 3D giant covalent structure. The theory underlying this thermodynamic control has been detailed previously[12,13]. In brief, crystallization within a microemulsion can only proceed by an existing crystal nucleus within a droplet gaining access to more growth material during transient dimer formation with another colliding droplet. If no pre-existing nuclei are present, no crystal growth occurs. Consequently, the ability to form a stable crystal nucleus becomes the determining factor governing whether crystallization proceeds at low supersaturation: thermodynamic control is thereby achieved. Factors that favour silica dissolution events over silica formation, particularly low SMS concentrations and high alkalinity, would be expected to induce thermodynamic control and thus produce α-quartz nanocrystals. In contrast, higher SMS concentrations will favour kinetic control and the formation of amorphous silica because the nanoconfined solutions are now supersaturated with respect to amorphous silica as well as quartz, and amorphous silica forms far more rapidly. Similarly, larger droplets will typically contain more SMS ions and lead to kinetic control because larger amorphous silica nanoparticles can form rapidly and persist. All this is in accordance with our observations.

The striking difference between organic molecule crystallization in microemulsions and the present system is that the silica nanoparticle growth and dissolution occur via the creation and breaking of covalent bonds rather than weaker intermolecular interactions in organic crystals. Adventitiously, the required Si–O bond breakage and formation is facilitated by the large fluctuations in alkalinity in the droplets as they exchange hydroxyl and (much more rarely) hydronium ions during energetic droplet collisions that produce transient dimers (see Supplementary Note 3). The large fluctuations in alkalinity result in repeated nanocrystal growth and dissolution steps, aiding thermodynamic control. Hence α-quartz nanocrystals are selectively obtained. Note that the sodium cations and effects arising from water confinement may also impact on the nanocrystal growth and dissolution steps; elucidating the significance of these factors requires further study. It is well-known that ≈2 nm amorphous silica particles can be formed by acidifying high pH silica solutions[30–32]. In stark contrast, our microemulsion methodology enables the crystallization of 1–5 nm α-quartz under ambient conditions from low concentration SMS solutions without the need for added acid. To our knowledge, this is the first time nanoquartz has been obtained from a non-biological route under ambient conditions.

The 1–5 nm nanocrystals synthesised from the microemulsions have a perturbed bulk-quartz structure but none-the-less have sufficient crystallinity to act as effective seeds for the hydrothermal synthesis of larger (<10 nm) quartz nanocrystals under mild conditions of 175 °C and autogenic pressure. The nanocrystals slowly grow and anneal over time, readily enabling nanoquartz of defined size and structure to be obtained exclusively by changing reaction times. These nanocrystals, free from growth modifiers or other contaminants, are ideal for studies aimed at elucidating the harmful role that silica crystallinity plays in inducing lung diseases such as silicosis. Furthermore, our two-stage microemulsion-hydrothermal methodology allows a significant control over the structure of sub-10 nm particles. Consequently, adopting this methodology for nanocrystal catalysts could help optimize their performance.

Methods

Materials. Chemicals were used as supplied and were as follows: sodium metasilicate nonahydrate (SMS) (≥98%, Aldrich), Span®80 (sorbitan monooleate) (Sigma-Aldrich), Brij® 30 (polyoxyethylene (4) lauryl ether) (Acros Organics), Triton X-114 (polyoxyethylene *tert*-octylphenyl ether, $C14H22O(C2H4O)_n$, n~7.5) (Sigma-Aldrich), heptane (≥99% Acros Organics), cyclohexane (99% GLC Specified, Fisher Scientific), methanol (99.99%, Fisher Scientific), acetone (99.98%, Fisher Scientific), ethyl acetate (99.92%, Fisher Scientific), sodium hydroxide (> 97% Laboratory reagent grade, Fisher Scientific), chloroform-deuterated (> 99.8 atom % D, Apollo Scientific), acetylacetone (99 + %, Acros Organics), aniline (99%, Sigma-Aldrich), 7 nm fumed silica (Sigma-Aldrich), 200-300 nm fumed silica (Sigma-Aldrich) and quartz standard certified reference material BCR®- 068 (Sigma-Aldrich). Ultra-high purity (UHP) water with a resistivity of 18.2 MΩ cm was obtained from a Sartorius arium® comfort water purifier system.

Nanoquartz synthesis in microemulsions. The microemulsions used either a surfactant combination of 1:1 wt.% Span® 80 and Brij® 30 in heptane at a surfactant: heptane ratio of 40:60 wt.%, or a surfactant solution comprising 30 wt.% Triton X-114 in cyclohexane. The microemulsions using Span® 80 and Brij® 30 are denoted with the prefix SB whilst the microemulsions using Triton X-114 have the prefix TX. Microemulsions were prepared by adding sodium metasilicate (SMS) solutions to the surfactant solutions followed by thorough mixing by vigorous hand-shaking to achieve a single transparent, homogeneous phase. The volume of SMS solution added to the surfactant solutions was varied from 5 µl to 50 µl per gram of surfactant solution with the 5 µl g^{-1} microemulsions providing the optimal results; the composition of these microemulsions, on the 2-g scale, are listed in the Supplementary Tables 2 and 3 for the Span® 80 / Brij® 30 and Triton X-114 surfactant systems, respectively. The microemulsions were typically left to stand for 2 days, though extended periods of 9 days and longer were also used on occasion. Thereafter, small aliquots from the microemulsions were pipetted onto a holey carbon film on a 300 mesh copper TEM grid (Agar Scientific), left to dry, washed with heptane (SB microemulsions) or cyclohexane (TX microemulsions) and then an acetone and water solution containing 75 wt.% acetone to remove the majority of the residual surfactant. The TEM grids were left to dry before examination using TEM.

Larger scale 400 g microemulsions were prepared containing 2.5 wt.% SMS aqueous solution to extract sufficient α-quartz nanocrystals for XRD, FTIR and ^{29}Si ssNMR analysis. On this larger scale, a slight cloudiness was often evident due to solid impurities in the surfactants. This cloudiness dissipated as the impurities precipitated after 2 days. Further 2 g additions of 2.5 wt.% SMS solution were added to the microemulsions after 2 and 4 days. After 2 weeks the precipitated nanoquartz was washed in a 1:1 solution of methanol and ethyl acetate (300 ml) via sonication in an ultrasound water bath for 30 min to remove residual surfactant and impurities. The purified nanoquartz was extracted by centrifugation at 9418 G (9000 revs per minute) for 10 min and left to dry in an oven at 60 ºC for 24 h.

The SMS used was only 98.5 wt.% pure, and although the FTIR spectrum of the insoluble SMS residue indicated the impurities consisted mainly of calcium carbonate with a broad peak at 1435 cm^{-1} and sharper peak at 880 cm^{-1}, it is clearly vital to verify that the nanoquartz was not, in fact, a minority impurity in the SMS starting material. Accordingly, we also used SMS solutions made by dissolving fumed silica in aqueous sodium hydroxide to prepare our microemulsions. There was no detectable difference between the nanoquartz synthesized from these microemulsions and those obtained from using the 98.5 wt.% SMS silica source.

Nanoquartz characterization. TEM analysis was performed on the nanoquartz samples using a JEOL 2100 F field emission gun TEM (FEG TEM) operating at 200 kV, a ZrO/W (100) Schottky Field Emission analytical emission microscope, in combination with an Oxford INCAx-Sight Si(Li) detector for Energy-Dispersive X-ray (EDX) spectroscopy and a Gatan Orius CCD camera. Phase contrast high resolution electron microscopy (HREM) was used to image nm-sized crystals. The structure of an individual nanocrystal was determined by indexing the fast Fourier transform (FFT) and selected area diffraction patterns.

Small Angle X-ray Scattering (SAXS) measurements were performed on the microemulsions using our in-house Bruker Nanostar, with cross-coupled Göbel mirrors and pin-hole collimation, using a sealed tube X-ray source operated at 40 kV and 35 mA to produce the Cu K_α radiation with a wavelength of 1.54 Å. The SAXS camera was fitted with a Hi-star 2D multiwire detector. Samples were contained in 2 mm glass capillaries. The optics and sample chamber were under vacuum to minimize air scatter. Scattering files were background subtracted using a capillary filled with the microemulsions' continuous phase and were then integrated to give the one-dimensional scattering intensity function $I(q)$, where q is the length of the scattering vector, defined by $q=(4\pi/\lambda)\sin\theta$, λ is the wavelength and 2θ is the scattering angle. The sample to detector distance was 650 mm, which provided a q range of 0.2–3.2 nm^{-1}. GIFT analysis[24] of the scattering function was used to obtain the pair distance distribution function $p(r)$ and a mean size for the droplets' hydrophilic core, see Supplementary Fig. 4 and Supplementary Tables 4 and 5. Details of this GIFT analysis procedure have been outlined previously[15,16].

Powder X-Ray Diffraction (PXRD) was performed on the nanoquartz using a Bruker D8 Advance operated at 40 kV and 40 mA to produce Cu K_α radiation. The experimental set-up was conducted within the DIFFRAC.SUITE software. Samples were ground with a spatula and placed on a glass XRD slide. The sample was subjected to a 6 mm × -ray beam width and was continuously rotated through 360º to reduce preferential orientation effects. Angles were scanned with the knife edge in place between $2\theta = 3$–80º at increments of 0.02º with the beam exposed at each angle for 1 s.

Thermogravimetric analysis (TGA) was performed on the nanoquartz using a Perkin-Elmer Pyris 1 TGA using air as the carrier gas. Samples were heated at a rate of 10 °C min^{-1} to 800 °C, where they were held for 60 min.

Fourier Transform Infrared (FTIR) spectra of the nanoquartz were recorded on a Pekin-Elmer Frontier FT-IR spectrometer equipped with a U-ATR sampling accessory and cesium iodide optics. 16 scans were collected for each sample at a resolution of 2 cm^{-1} over a wavenumber region of 4000 cm^{-1} to 380 cm^{-1}.

Solid-state ^{29}Si Magnetic Resonance (ssNMR) spectra of the nanoquartz were recorded at 79.44 MHz using a Varian VNMRS spectrometer and a 6 mm (rotor o.d.) magic-angle spinning probe. They were obtained using direct excitation with a 300 s recycle delay at ambient probe temperature (~25 °C) and at a sample spin-rate of approximately 6 kHz. Between 200 and 240 repetitions were accumulated. Spectral referencing was with respect to an external sample of neat tetramethylsilane (carried out by setting the high-frequency signal from tetrakis (trimethylsilyl)silane to −9.9 ppm).

^{1}H Nuclear Magnetic Resonance spectra of the catalysis reaction mixture containing acetylacetone, aniline and 4-(phenylamino)-pent-3-en-2-one in chloroform were recorded on a Bruker Advance III spectrometer with operating frequency of 400.13 MHz. Chemical shift values were recorded in ppm, using residual protic solvent as an internal standard.

Hydrothermal synthesis experiments. Hydrothermal synthesis experiments were conducted at 175 °C for 1–7 days using 237.4 mg of fumed silica in 0.1 M SMS together with 57.4 mg of seeds consisting of either (i) the nanoquartz synthesized from the 400-g scale microemulsions or (ii) fumed silica for the control experiments. The 237.4 mg of fumed silica in 0.1 M SMS was heated to 90 °C to dissolve the fumed silica before adding to the seeds in the hydrothermal unit, sealing the unit and then heating to 175 °C. After the hydrothermal unit had cooled, acetone was added to the hydrothermal product, present as a sedimented hydrated cake, to aid extraction from the hydrothermal unit. This was followed by centrifugation at 9418 G (9000 revs. per min.) for 10 min to recover the product. The sediment was dried in an oven at 60 °C for 24 h, producing a cake that was then ground with a spatula to give nanoquartz powders.

Catalysis studies. Acetylacetone (3 mmol), aniline (3 mmol), and 18 mg of nanoquartz particles (10 mol%) were placed in a glass vial and sonicated in an ultrasonic bath for 6 h, during which time the water bath temperature was raised to 55 °C. 10 µl of the resulting mixture was pipetted into 750 µl of chloroform for ^{1}H NMR analysis. The yield of the product, 4-(phenylamino)-pent-3-en-2-one, was determined at 4, 5, and 6 h from the ratio of the reactant, aniline, triplet of triplets at 6.76 ppm and the product, 4-(phenylamino)-pent-3-en-2-one, singlet at 5.19 ppm (see Supplementary Fig. 9), since both of these signals correspond to one proton. Note that acetylacetone exists as enol and keto tautomeric forms in equilibrium, with the ratio of these two forms essentially unchanged within experimental error (enol:keto approximately 9:2, see peaks H and J in Supplementary Fig. 9) throughout the experiments.

^{1}H NMR (400 MHz, $CDCl_3$) characterization data. Aniline: δ 3.60 (brs, 2 H), 6.69 (dt, 2 H), 6.76(tt, 1 H), 7.16(td, 2 H). Acetylacetone: δ 2.05 (s, 6 H), 2.24 (s, 6 H), 3.59 (s, 2 H), 5.50 (s, 1 H). 4-(phenylamino)-pent-3-en-2-one: δ 1.99 (s, 3 H), 2.10 (s, 3 H), 5.19 (s, 1 H), 7.10-7.36 (m, 5 H), 12.47 (brs, 1 H).

Data availability. All the data generated or analysed during this study are included in this published article (and its electronic supplementary material files).

Received: 14 May 2018 Accepted: 3 August 2018
Published online: 24 August 2018

References

1. Sochalski-Kolbus, L. M. et al. Solvothermal synthesis and surface chemistry to control the size and morphology of nanoquartz. *Cryst. Growth Des.* **15**, 5327–5331 (2015).
2. Jiang, X., Jiang, Y.-B. & Brinker, C. J. Hydrothermal synthesis of monodisperse single-crystalline alpha-quartz nanospheres. *Chem. Commun.* **47**, 7524–7526 (2011).
3. Bertone, J. F., Cizeron, J., Wahi, R. K., Bosworth, J. K. & Colvin, V. L. Hydrothermal synthesis of quartz nanocrystals. *Nano Lett.* **3**, 655–659 (2003).
4. Pastero, L., Turci, Leinardi, R., Pavan, C. & Monopoli, M. Synthesis of α-quartz with controlled properties for the investigation of the molecular determinants in silica toxicology. *Cryst. Growth Des.* **16**, 2394–2403 (2016).
5. Carretero-Genevrier, A. et al. Soft-chemistry–based routes to epitaxial α -quartz thin films with tunable textures. *Science* **340**, 827–831 (2013).

6. Drisko, G. L. et al. Crystallization of hollow mesoporous silica nanoparticles. *Chem. Commun.* **51**, 4164–4167 (2015).
7. Matsuno, T. et al. A single-crystalline mesoporous quartz superlattice. *Angew. Chem. Int. Ed.* **55**, 6008–6012 (2016).
8. Bansal, V., Ahmad, A. & Sastry, M. Fungus-mediated biotransformation of amorphous silica in rice husk to nanocrystalline silica. *J. Am. Chem. Soc.* **128**, 14059–14066 (2006).
9. Mackenzie, F. T. & Gees, R. Quartz: synthesis at Earth-surface conditions. *Science* **173**, 533–535 (1971).
10. Stöber, W., Fink, A. & Bohn, E. Controlled growth of monodisperse silica spheres in the micron size range. *J. Colloid Interface Sci.* **26**, 62–69 (1986).
11. Wang, X.-D. et al. Preparation of spherical silica particles by Stöber process with high concentration of tetra-ethyl-orthosilicate. *J. Colloid Interface Sci.* **341**, 23–29 (2010).
12. Nicholson, C. E., Chen, C., Mendis, B. & Cooper, S. J. Stable polymorphs crystallized directly under thermodynamic control in three-dimensional nanoconfinement: a generic methodology. *Cryst. Growth Des.* **11**, 363–366 (2011).
13. Chen, C., Cook, O., Nicholson, C. E. & Cooper, S. J. Leapfrogging Ostwald's rule of stages: crystallization of stable γ-glycine directly from microemulsions. *Cryst. Growth Des.* **11**, 2228–2237 (2011).
14. Nicholson, C. E. & Cooper, S. J. Crystallization of mefenamic acid from dimethylformamide microemulsions: obtaining thermodynamic control through 3D nanoconfinement. *Crystals* **1**, 195–205 (2011).
15. Chen, C., Nicholson, C. E., Ramsey, H. E. & Cooper, S. J. Non-classical crystallisation of dipicolinic acid in microemulsions. *Cryst. Growth Des.* **15**, 1060–1066 (2015).
16. Hargreaves, N. J. & Cooper, S. J. Nanographite synthesized from acidified sucrose microemulsions under ambient conditions. *Cryst. Growth Des.* **16**, 3133–3142 (2016).
17. Gan, L. M., Zhang, K. & Chew, C. H. Preparation of silica nanoparticles from sodium orthosilicate in inverse microemulsions. *Colloids Surf. A* **110**, 199–206 (1996).
18. Arriagada, F. J. & Osseo-Asare, K. Synthesis of nanosize silica in a nonionic water-in-oil microemulsion: effects of the water/surfactant molar ratio and ammonia concentration. *J. Colloid Interface Sci.* **211**, 210–220 (1999).
19. Zhang, K., Gan, L. M., Chew, C. H. & Gan, L. H. Silica from hydrolysis and condensation of sodium metasilicate in bicontinuous microemulsions. *Mater. Chem. Phys.* **47**, 164–170 (1997).
20. Jesionowski, T., Tepper, B. & Krysztafkiewicz, A. Characterisation of spherical silicas obtained from sodium silicate and hydrochloric acid in emulsion medium using hexane as the organic phase. *Surf. Interface Anal.* **39**, 948–957 (2007).
21. Turci, F. et al. Revisiting the paradigm of silica pathogenicity with synthetic quartz crystals: the role of crystallinity and surface disorder. *Part. Fibre Toxicol.* **13**, 32 (2016).
22. Pitts, J. R. & Czanderna, A. W. Reduction of silica surfaces with particle beams. *Nucl. Instrum. Method Phys. Res.* **B13**, 245–249 (1986).
23. Kubicki, J. D., Sofo, J. O., Skelton, A. A. & Bandura, A. V. A new hypothesis for the dissolution mechanism of silicates. *J. Phys. Chem. C* **116**, 17479–17491 (2012).
24. Brunner-Popela, J. & Glatter, O. Small-angle scattering of interacting particles. I. Basic principles of a global evaluation technique. *J. Appl. Cryst.* **30**, 431–442 (1997).
25. Miehe, G. & Graetsch, H. Crystal structure of moganite: a new structure type for silica. *Eur. J. Mineral.* **4**, 693–706 (1992).
26. Zhang, M. & Moxon, T. Infrared absorption spectroscopy of SiO_2-moganite. *Am. Mineral.* **99**, 671–680 (2014).
27. Graetsch, H., Topalovic, C. & Gies, H. NMR spectra of moganite and chalcedony. *Eur. J. Mineral.* **6**, 459–464 (1994).
28. Alinezhad, H., Tajbakhsh, M., Sarkati, M. N. & Zare, M. Nano-SiO_2 catalyzed synthesis of β-enaminones under solvent free conditions. *Mon. Chem.* **147**, 1591–1596 (2016).
29. Gholap, A. R., Chakor, N. S., Daniel, T., Lahoti, R. J. & Srinivasan, K. V. A remarkably rapid regioselective synthesis of β-enaminones using silica chloride in a heterogeneous as well as an ionic liquid in a homogeneous medium at room temperature. *J. Mol. Catal. A Chem.* **245**, 37–46 (2006).
30. Rimer, J. D., Lobo, R. F. & Vlachos, D. G. Physical basis for the formation and stability of silica nanoparticles in basic solutions of monovalent cations. *Langmuir* **21**, 8960–8971 (2005).
31. Carcouet, C. C. M. C. et al. Nucleation and growth of monodisperse silica nanoparticles. *Nano Lett.* **14**, 1433–1438 (2014).
32. Fedeyko, J. M., Vlachos, D. G. & Lobo, R. F. Formation and structure of self-assembled silica nanoparticles in basic solutions of organic and inorganic cations. *Langmuir* **21**, 5197–5206 (2005).

Acknowledgements

This work was supported by the Engineering and Physical Sciences Research Council (EPSRC) Centre for Doctoral Training in Soft Matter and Functional Interfaces (grant EP/L015536/1) and by EPSRC and GSK through an Industrial CASE award (grant EP/I501355/1). We thank B. Mendis, D. Apperley, and H. Riggs for TEM, ssNMR, and SAXS assistance, respectively, and R. Thompson for reviewing the manuscript prior to submission.

Author contributions

S.C. conceived the concept, supervised the work plan and wrote the manuscript. N.H. performed the ambient temperature studies on the microemulsions of varying size and SMS concentration, P.B. performed the scaled-up studies on the microemulsions, the hydrothermal synthesis work and the catalyst studies.

Additional information

Supplementary information accompanies this paper at https://doi.org/10.1038/s42004-018-0049-4.

Competing interests: The authors declare no competing interests.

Reprints and permission information is available online at http://npg.nature.com/reprintsandpermissions/

Publisher's note: Springer Nature remains neutral with regard to jurisdictional claims in published maps and institutional affiliations.